

SOFIA FAR-INFRARED [O III] AND [O I] OBSERVATIONS OF DENSE CO-KNOTS IN THE SUPERNOVA REMNANT CASSIOPEIA A: MULTI-PHASE EJECTA

JEONGHEE RHO¹, SOFIA H. J. WALLSTRÖM^{2, 3}, SÉBASTIEN MULLER⁴, ISABELLE CHERCHNEFF⁵, DARIO FADDA⁶, OLIVIER BERNÉ^{7, 8}, JOHN H. BLACK⁴, ALEXANDER G. G. M. TIELENS⁹

ABSTRACT

Dense, fast-moving ejecta knots in supernova remnants are prime sites for molecule and dust formation. We present SOFIA far-IR spectrometer FIFI-LS observations of CO-rich knots in Cas A which cover a ~ 1 square arc minute area of the northern shell, in the [O III] 52 and $88\mu\text{m}$ and [O I] $63\mu\text{m}$ lines. The FIFI-LS spectra reveal that the line profiles of [O III] and [O I] are similar to those of the *Herschel* PACS [O III] and CO lines. We find that the [O III] maps show very different morphology than the [O I] map. The [O III] maps reveal diffuse, large-scale structures and the ratio of the two [O III] lines imply the presence of gas with a range of density $500 - 10,000 \text{ cm}^{-3}$ within the mapped region. In contrast, the [O I] map shows bright emission associated with the dense CO-rich knots. The $63\mu\text{m}$ [O I] line traces cooled, dense post-shocked gas of ejecta. We find that IR-dominated [O III] emission is from post-shocked gas based on its morphology, high column density, and velocity profile. We describe multi-phase ejecta knots, a lifetime of clumps, and survival of dust in the young supernova remnants.

Subject headings: astrochemistry: oxygen - infrared: supernova remnants - ISM: individual objects (Cas A) - dust: shock waves

1. INTRODUCTION

Massive stars ($>8 M_{\odot}$) eject much of the elements synthesized over its lifetime back into the interstellar medium (ISM) at the end of its lifetime. This is one of the main ways in which a galaxy's metallicity is increased, thereby enriching the next generation of stars and planets (Pagel 1997). Supernova are also a main source of kinetic energy for the ISM, stirring up the gas, providing turbulent support to the ISM and processing interstellar dust through powerful shocks (Tielens 2005). Instabilities create dense clumps in the ejecta (Hammer et al. 2010) and hundreds of such dense Fast Moving Knots (FMKs) are commonly observed in type II supernova remnants (SNRs), containing a substantial fraction of the supernova ejecta and its kinetic energy (Fesen 2001). The high density of these knots is conducive to molecule and dust formation (Sarangi & Cherchneff 2015; Sluder et al. 2018). However, whether dust can survive the reverse shock is still not clear (Nozawa et al. 2007; Nath et al. 2008; Silvia et al. 2012; Biscaro & Cherchneff 2016).

Understanding the formation and survival of supernova dust has gotten additional impetus with the recent *Herschel* detection of copious amounts of dust in SNRs, Cas A ($0.1-0.6M_{\odot}$), SN 1987A ($0.5M_{\odot}$) and G54.1+0.3 ($0.1-0.9M_{\odot}$) (Barlow et al. 2010; De Looze et al. 2017; Matsuura et al. 2011; Rho et al. 2018), as well the detection of copious amounts of dust in the early universe (Laporte et al. 2017; Spilker et al. 2018), which is often ascribed to injection by supernovae (Pei et al. 1991; Cherchneff & Dwek 2010). Understanding the characteristics of dense knots in SNRs and their interaction with the reverse shock and eventual dispersion and merging with the ISM is therefore a key question for the evolution of galaxies and the cosmic history of dust.

Cassiopeia A (Cas A) is one of the youngest Galactic SNRs with an age of ~ 350 yr and its progenitor is believed to be a Wolf-Rayet star with a mass of $15-25 M_{\odot}$ (Krause et al. 2008). [O I] observation was reported by Docenko & Sunyaev (2010, DS10) with ISO/LWS. The *Herschel Space Observatory* detected $88\mu\text{m}$ [O III] lines, and high-J rotational CO lines (Wallström et al. 2013, W13). We report [O I] and [O III] maps toward the northern part of Cas A over a ~ 1 square arc minute with SOFIA Field-Imaging Far-Infrared Line Spectrometer (FIFI-LS), and this letter is one of the first observations with FIFI-LS.

2. OBSERVATIONS

We have targeted a region in the north of Cas A with FIFI-LS on the SOFIA 2.5-m telescope, for the lines of [O III] at 52 and $88\mu\text{m}$ and [O I] at $63\mu\text{m}$. The observations covered two partially overlapping $30'' \times 30''$ regions as shown in Figure 1a where two observations of NW (knot2) and SE (knot1) fields were combined. The SE location (knot1) is first recognized as Ne-rich crescent-shaped (a.k.a. Ne moon) region (Ennis et al. 2006), and CO-rich knots (see Fig. 4 of Rho et al. 2012). The [O III] at $52\mu\text{m}$ and $88\mu\text{m}$, and [O I] at $63\mu\text{m}$ observations took

¹ SETI Institute, 189 N. Bernardo Ave, Mountain View, CA 94043; jrho@seti.org

² Institute of Astronomy, KU Leuven, Celestijnenlaan 200D bus 2401, 3001 Leuven, Belgium

³ Institute of Astronomy and Astrophysics, Academia Sinica, 11F of Astronomy-Mathematics Building, No.1, Sec. 4, Roosevelt Rd., Taipei 10617, Taiwan

⁴ Department of Space, Earth and Environment, Chalmers University of Technology, Onsala Space Observatory, SE-43992 Onsala, Sweden

⁵ Instituto de Física Fundamental Consejo Superior de Investigaciones Científicas (CSIC), Serrano 113 bis 28006, Madrid Spain; i.cherchneff@iff.csic.es

⁶ SOFIA Science Center/USRA, NASA Ames Research Center, M.S. N232-12, Moffett Field, CA 94035

⁷ Université de Toulouse, UPS-OMP, IRAP, 31028 Toulouse, France

⁸ CNRS, IRAP, 9 Av. Colonel Roche, BP 44346, 31028 Toulouse Cedex 4, France

⁹ Leiden Observatory, Leiden University, PO Box 9513, 2300 RA Leiden, The Netherlands

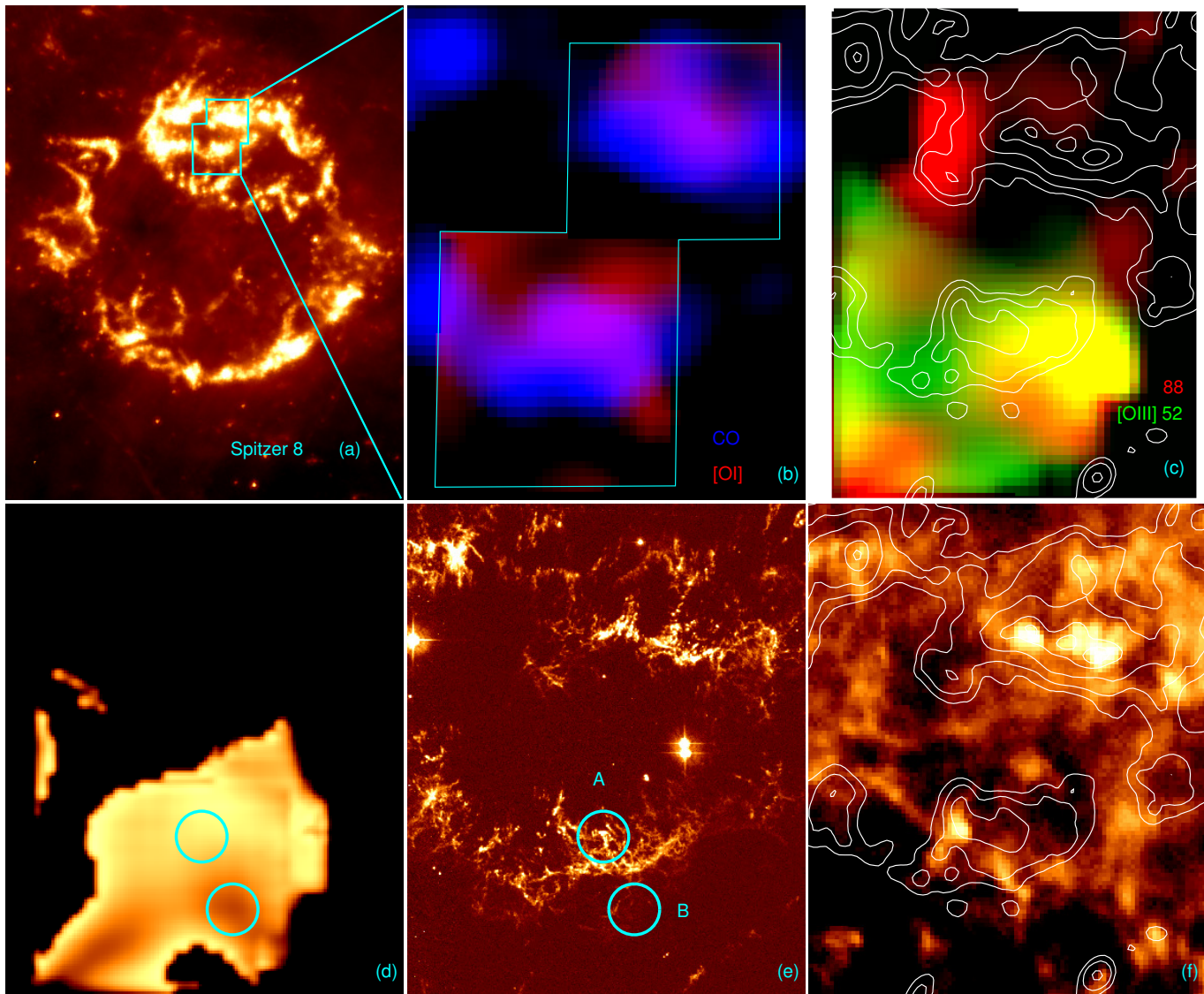


FIG. 1.— (a) The field of view (FOV) of SOFIA FIFI-LS observations (polygon in cyan, covering $1'$ area) is marked on *Spitzer* $8\mu\text{m}$ map of Ar ejecta in Cas A (Rho et al. 2008). The image covers $4.7' \times 6.2'$ centered on R.A. $23^{\text{h}}23^{\text{m}}25.82^{\text{s}}$ and Dec. $+58^{\circ}48'50.42''$ (J2000). (b) Zoomed image of Cas A ($1' \times 1'$ FOV, the polygon is the same as in panel (a)) centered on the SOFIA FIFI-LS $63\mu\text{m}$ [O I] image (the flux ranges $0.035\text{--}0.70$ Jy/ $1''$ pixel) is superposed on *Spitzer* CO map at $4.5\mu\text{m}$ which was smoothed to the same resolution. The panels (c, d, e) cover the same FOV. (c) Mosaicked [O III] emission image at $52\mu\text{m}$ (in green, the flux ranges $0.1\text{--}0.63$ Jy/pixel) and $88\mu\text{m}$ (in red; the flux ranges $0.01\text{--}0.08$ Jy/pixel). The white contours are *Spitzer* $8\mu\text{m}$ Ar image from Rho et al. (2008). (d) The ratio map of [O III] emission (using the pixels with $S/N > 5$) is derived between $52\mu\text{m}/88\mu\text{m}$ emission. The scale of the ratio ranges from ~ 2 to 9 (brighter color with a higher value) which correspond to a density from 500 to a few times of 10^4 cm^{-3} (see the text and Fig. 3). Two circles indicate the [O III] optical-bright/IR-dim ejecta region (“Region A” with the ratio $52/88\mu\text{m} \sim 8$) and IR-bright/optical-dim (“Region B” with the ratio $52/88\mu\text{m} \sim 2$) regions marked on the ratio map (d) and *HST* optical [O III] image (e). (f) *Chandra* X-ray image is superposed on *Spitzer* $8\mu\text{m}$ contours, showing that X-ray gas is anti-correlated to the IR- $8\mu\text{m}$ ejecta in the south although the X-ray ejecta have IR counterparts in the north.

place on 2014 April 26, and additional observations for the [O III] at 52 and $88\mu\text{m}$ took place on 2015 October 14 and 21 (PROG.ID of 02.0058 and 03.0051; PI. Tielens). The on-source exposures are 69, 86, and 43 min for [O I] $63\mu\text{m}$, [O III] 52 and $88\mu\text{m}$, respectively. A chopping/nodding mode was used with a chop throw of $300''$, and FIFI-LS covers a field of view (FOV) of $30'' \times 30''$ in the lines we present. FIFI-LS spectral cube has a sampling with a pixel size of $1''$, and the spatial resolution of the blue ($51\text{--}120\mu\text{m}$) channel is $6''$ (Colditz et al. 2018) because of a better spatial sampling and more efficient dithering than the default spectroscopy mode of Herschel PACS (W13). The pointing stability of SOFIA is better

than $0.4''$ (Temi et al. 2018). The data used is the FIFI-LS pipeline version of 1.3_3 produced by SOFIA Science Center.

FIFI-LS calibration uncertainty on the blue channel is at 15% level, and line observations are corrected for atmospheric absorption and telluric features by the SOFIA FIFI-LS team using ATRAN models. We checked the atmospheric transmission (>0.8) curve for each line, and the primary line structures and fluxes are not significantly affected but it may add some uncertainty ($<20\%$). The spectral cube was reduced using the Python GUI

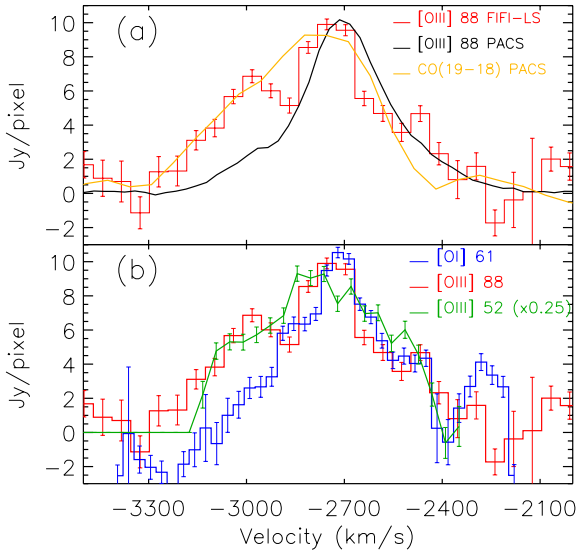


FIG. 2.— The FIFI-LS spectrum of [O III] at $88\mu\text{m}$ extracted from an area of $9''$ pixel (a) is compared with that of *Herschel* PACS $88\mu\text{m}$ [O III] and CO(19-18) (W13); the spectra show similar line profiles. (b) SOFIA FIFI-LS spectrum of $63\mu\text{m}$ [O I] is compared with the 88 and $52\mu\text{m}$ [O III] spectra.

software *SOSPEX*¹⁰ (Fadda & Chambers 2018). We obtained consistent results by using the other data reduction methods such as “fluxer”¹¹ and our own IDL extraction routines.

3. RESULTS

We extracted FIFI-LS spectra from the central area (a $9'' \times 9''$ area centered on R.A. $23^{\text{h}}23^{\text{m}}24.9^{\text{s}}$ and Dec. $+58^{\circ}50'03.3''$, J2000) of the PACS observations (W13) as shown in Figure 2. The surface brightness of [O I] and [O III] lines listed in Table 1A are comparable to those from ISO (a beam size of $80''$, # 2 of DS10) and PACS (W13) within a factor of 1.2-2.6.

For detailed comparison, we extracted PACS $88\mu\text{m}$ [O III] spectra from archival data to match the exact extraction area of two different missions and instruments. We note that recently processed PACS data (version v14.2.0) yield fainter brightness (in Table 1) than the one by Wallström et al. (2013). The FIFI-LS $88\mu\text{m}$ [O III] line brightness is 60% smaller than that of the PACS spectrum and the line profiles show $400\text{--}600\text{ km s}^{-1}$. We use 60% as our systematic uncertainty of the brightness, which would not change our main science results considering that the SNR is a diffuse source.

We present velocity integrated maps (the velocity range is from -3300 to -2400 km s^{-1} ; see Fig. 2) of [O I] 63 , [O III] 52 and $88\mu\text{m}$ maps in Figure 1. The $88\mu\text{m}$ FIFI-LS map is consistent with that of PACS although the existing PACS data have only 25 spatial pixels as the region was undersampled. Both 88 and $52\mu\text{m}$ [O III] maps show very different structure from the [O I] map. The [O I] $63\mu\text{m}$ map reveals clumpy structures and bright emission associated with the dense ejecta and CO-rich knots (Rho et al. 2008) in Figure 1b. In contrast, the [O III] 52 and $88\mu\text{m}$ maps show mostly diffuse, large-scale

structures and bright emission clearly present outside of the region of dense ejecta knots in Figure 1c. The $63\mu\text{m}$ [O I] line is 50% brighter than the $88\mu\text{m}$ [O III] line and 22% of $52\mu\text{m}$ [O III] brightness, as listed in Table 1A.

We estimated the ratio of [O III] 52 and $88\mu\text{m}$ maps since the ratio is a density indicator (see Fig. 3 and discussion below). We used the pixels with positive values for both 52 and $88\mu\text{m}$ emission, where the NW regions (knot2) within the observed FOV show weak [O III] emission. We find ratios between ~ 2 and ~ 9 (Fig. 1d).

4. DISCUSSION

High-J CO emission with *Herschel* (W13) together with *Spitzer*, AKARI, and ground-based IR studies (Rho et al. 2009, 2012) of dense clumps in Cas A have revealed large column densities ($4 \times 10^{17}\text{ cm}^{-2}$) of warm, dense CO gas (W13). The theoretical model of Biscaro & Cherchneff (2014) suggested that CO molecules are destroyed in the reverse shock but rapidly reformed in the postshock gas. As a result of the large density contrast between the dense knots and their surroundings, the reverse shock driven into the knots is relatively weak and dust can survive in the CO-rich gas. Morphologically, the $63\mu\text{m}$ [O I] emission (Fig. 1b) is closely related to dense ejecta/CO-knot emission. The [O I] line traces cooled, dense post-shocked gas of ejecta and the luminosity of [O I] for $9'' \times 9''$ area is $0.5 L_{\odot}$. Because of its high critical density, the [O I] emission likely arises from very dense ($\sim 10^{5-6}\text{ cm}^{-3}$) post-shock gas, with a high column density of $2 \times 10^{15}\text{ cm}^{-2}$ (Table 1A); these physical properties are consistent with the theoretical shock models (Borkowski & Shull 1990, DS10).

Based on the energy levels of the ground-state atomic fine structure, the ratios of [O III] lines constrain the density and temperature of the emitting region, independent of the geometry. We generated the set of [O III] IR line ratio between $52\mu\text{m}$ and $88\mu\text{m}$ with a grid of density and temperature (see Reach & Rho 2000) and the line diagnostic model (see also Osterbrock 1988) is shown in Figure 3. The IR [O III] line ratio between [O III] $52\mu\text{m}$ and $88\mu\text{m}$ ranges from 2 to 9, and the IR [O III] line diagnostic implies a density range of $300 - 5 \times 10^4\text{ cm}^{-3}$ (and a temperature $> 100\text{ K}$). The ratio map in Figure 1d corresponds to a density map, indicating a higher density at the ejecta and neighboring region, but the ratio map differs from the ejecta map.

The [O III] far-IR morphology of $52\mu\text{m}$ and $88\mu\text{m}$ emission in Figure 1c differs from the dense ejecta emission seen in optical [O III], infrared Ar ejecta, and $63\mu\text{m}$ [O I] emission. The optical [O III] emission at 5007Å shows bright knots at the ejecta position, and the optical [O III] is faint outside the ejecta (Figure 1e). The *HST* optical [O III] emission is found near the reverse shock and shocked gas from a cooling post-shock region (Fesen 2001; Morse et al. 2004).

What is the origin of far-IR [O III]? Itoh (1981) estimated 70% of $52\mu\text{m}$ [O III] is from shocked gas using a collisional ionization equilibrium (CIE) model, and the model by Sutherland & Dopita (1995) predicts bright [O III] below $20,000\text{ K}$. To understand the origin and physical condition of IR-emitting [O III] emission, we selected two regions, one (Region A, see Figs. 1d, 1e) with the high ratio of $52/88\mu\text{m}$ ($R(52/88)$) of ~ 8

¹⁰ <https://github.com/darioflute/sospex/>

¹¹ <http://www.ciserlohe.de/fluxer/fluxer.html>

TABLE 1
SPECTRAL LINE BRIGHTNESSES OF OBSERVED LINES AND PHYSICAL PROPERTIES OF LINE EMITTING REGIONS

Table 1A	Wavelength bandwidth(μm)	Wavelength center (μm)	Shift (km s^{-1})	FWHM (μm)	FWHM (km s^{-1})	Surface Brightness ($\text{erg s}^{-1} \text{cm}^{-2} \text{sr}^{-1}$)
[O III]	51.27-51.56 (51.29-51.72) ^a	51.3357 \pm 0.0089	-2772 \pm 52	0.0924 \pm 0.0327	540 \pm 190	1.841 \pm 0.092 $\times 10^{-3}$
[O III]	87.04-88.05 (87.36-88.34)	87.5445 \pm 0.0150	-2755 \pm 51	0.1501 \pm 0.0260	514 \pm 89	2.700 \pm 0.117 $\times 10^{-4}$
[O III]	PACS ^a : 85.27-89.14	87.5594 \pm 0.0100	-2678 \pm 35	0.0960 \pm 0.0016	329 \pm 07	4.360 \pm 0.065 $\times 10^{-4}$
[O I]	62.41-62.96 (62.43-62.98)	62.6138 \pm 0.0127	-2706 \pm 61	0.0964 \pm 0.0447	461 \pm 214	4.027 \pm 0.328 $\times 10^{-4}$
Table 1B	Region ^b					
	5007 \AA ^c ($\text{erg s}^{-1} \text{cm}^{-2} \text{sr}^{-1}$)	52 μm ($\text{erg s}^{-1} \text{cm}^{-2} \text{sr}^{-1}$)	$R(52/88)$	$R(5007/52)$	$R(52/5007)$	$R(88/5007)$
A (Ejecta)	3.65 \pm 0.14 $\times 10^{-2}$	17.7 \pm 6.0 $\times 10^{-4}$	~ 8	20 \pm 7	0.05	0.006
B (IR-[O III])	4.60 \pm 0.50 $\times 10^{-3}$	8.2 \pm 4.1 $\times 10^{-4}$	~ 2	5.6 \pm 3.0	0.36	0.18
Table 1C	density	temperature	column density	ΔR ^d	Einstein A	Pressure
Emission	$n(\text{cm}^{-3})$	T (K)	(cm^{-2})	(cm)	(s^{-1})	(cm^{-3} K)
IR [O III] ^e	500	6600	10^{16}	$2 \times 10^{13}/f$	A(52)=9.8E-5	$\sim 3 \times 10^6$
Optical [O III] ^f	10^4	6000	10^{15}	$10^{11}/f$	A(5007)=2E-2	$\sim 1 \times 10^8$
IR [O I]	$\sim 10^6$...	2×10^{15}	$2 \times 10^9/f$	A(63)=8.9E-5	...
CO	10^6	400, 2000	5×10^{17}	$5 \times 10^{11}/f$...	(5-10) $\times 10^8$

^a The wavelength bandwidth in parenthesis is the coverage for the northwestern region.

^b Regions A and B are marked in Figure 1d and Figure 1e.

^c The optical flux is extinction corrected.

^d ΔR is the thickness of the emitting region and f is a filling factor.

^{e,f} “IR [O III]” is IR-bright and optical dim [O III] region estimated from “Region A”, and “Optical [O III]” is optical-bright and IR dim [O III] region estimated from “Region B”.

which coincides with dense ejecta (centered on R.A. 23^h23^m25.11^s and Dec. +58°50′02.8″), and the other (Region B) with the low $R(52/88)$ of ~ 2 which is outside the ejecta emission (centered on R.A. 23^h23^m24.64^s and Dec. +58°49′54.22″). “Region A” is the compact dense ejecta region, optical-[O III] bright and CO/[O I] emitting region, and “Region B” is IR-[O III] bright region. We have measured the brightness of [O III] 5007 \AA , 52 μm and 88 μm for a 6″ circular aperture. In Table 1B, the brightness and the ratios are listed. We used *HST* ACS F475W image which contains both 5007 and 4959 \AA lines (Fesen et al. 2006) and we assumed 3/4 of optical emission is from 5007 \AA [O III] line and the extinction is $A_v = 5.7$ mag (Hurford & Fesen 1996). When we compare the line ratios of $R(52/88)$ and $R(52/5007)$ with the line diagnostics in Figure 3, IR-[O III] bright regions (Region B) are dominated by gas with an electron density and temperature of $(n_e, T) = (500 \text{ cm}^{-3}, 6000 \text{ K})$. Optical-[O III] bright, dense knots (Region A) are dominated by gas with $(10^4 \text{ cm}^{-3}, 6600 \text{ K})$. The densities are much less than the densities from the CO observations (10^6 cm^{-3} , W13) or the density required to collisionally excite the [O I] line.

We compare the optical and IR [O III] with *Chandra* X-ray map. The optical [O III] emission is well correlated with the IR dense (Ar) ejecta from *Spitzer* IRAC 8 μm map. The X-ray gas appears outside the dense optical ejecta (Region A) as shown in Figures 1e and 1f and is in some degree associated with IR-[O III] bright region. Indications of ejecta knot mass stripping in Cas A have been reported (Fesen et al. 2011).

We estimated the oxygen column density and abundance of oxygen. The column density is $4\pi I/(A h\nu)$ for each line, where I is the surface brightness, A is the line Einstein A coefficient, h is the Planck constant, and ν is the frequency. We summarize the physical properties of

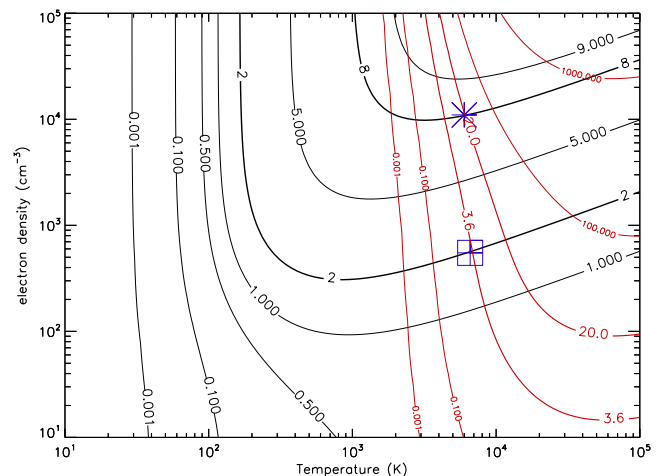


FIG. 3.— Line diagnostic contours of the ratios of IR [O III] 52 $\mu\text{m}/88\mu\text{m}$, a density indicator (black) and optical to IR ratios of [O III] between 5007 \AA and 52 μm (red). The observed ratios are marked with the thick solid lines. The model infers the bright ejecta region has a density of 10^4 cm^{-3} , and a temperature of 6000 K (marked as an asterisk), and the IR [O III] bright region has a density of 550 cm^{-3} and a temperature of 6600 K (a square).

IR [O III], optical [O III], IR [O I], and CO emitting regions in Table 1C. The column densities of 52 and 88 μm [O III] lines are of an order of 10^{16} cm^{-2} and are comparable to those of 63 μm [O I] line and optical emission.

Shock models predict bright [O III] emission arising from the preshock gas photo-ionized by the shock emission and the postshock cooling and recombining gas. Such regions are called Photo-Ionized Regions (PIR). It is tempting to associate the low density gas bright in the IR but not the optical [O III] lines (Region B) with the preshock PIR while the denser optically bright [O III] emission (Region A) would naturally arise from the post-

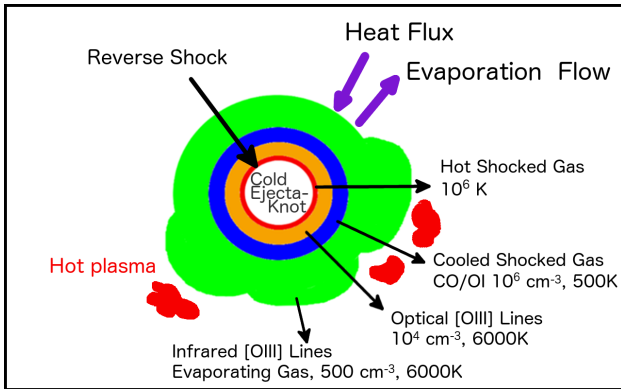


FIG. 4.— Cartoon of CO-rich ejecta knot with multi-phase [O I]/CO, IR [O III], optical [O III] and X-ray emitting layers. The marked physical conditions are only dominant emission for each. The patches in red are denser gas in X-rays.

shock gas (Fesen et al. 2011; Docenko & Sunyaev 2008). Given the uncertainties in the shock models, the observed IR-[O III] intensities and derived column densities, densities and temperatures are in good agreement with calculated post-shock models (Sutherland & Dopita 1995, DS10). However, the morphology of the [O III] emission is not in agreement with this interpretation. The PIR gas should be in the region interior to the reverse shock; e.g., deep within the FMK. Observationally, this gas is very diffuse and surrounds the dense clumps and, hence, it should be postshock gas. So, rather than PIR gas, we surmise that the IR bright/optically dim [O III] emitting gas is associated with the evaporating gas in the surfaces of the shocked clumps driven by electron conduction (Borkowski & Shull 1990). Another evidence that IR [O III] emission is post-shocked gas comes from the velocity information. The velocity profiles of [O III] are the same as that from shocked gas of $63\mu\text{m}$ [O I] line. Unshocked gas using *Spitzer* [O IV] line (from the central region) indicates the velocity for the gas toward us peaks at -2000 km s^{-1} . We expect to observe a difference in velocity between shocked and unshocked gas and this is not the case for IR [O III] lines as shown in Figure 2.

The observed CO and [O I] emission is most naturally associated with postshock gas that has had time to cool, recombine and form molecules (Biscaro & Cherchneff 2014). This gas is directly related therefore to the [O III] emitting gas. The pressure of the optically bright [O III] emitting gas is $\sim 10^8\text{ cm}^{-3}\text{ K}$ as summarized in Table 1C. This is a little less than the pressure derived from the CO observations of $5 \times 10^8\text{ cm}^{-3}\text{ K}$ (W13). The agreement in morphology supports this interpretation. In contrast, the low density, IR bright [O III] emitting gas has a gas pressure of $\sim 3 \times 10^6\text{ cm}^{-3}\text{ K}$; much less than the pressure of the postshock gas. Momentum conservation in the evaporating gas requires $\rho v^2 = P_{ps}$ with P_{ps} the pressure in the the postshock gas and where we have neglected the gas pressure in the flow. This results in a flow velocity of 3 km/s , or — as expected — about the sound speed, of an oxygen gas at 6000 K .

The mass loss rate of the clumps as measured by the evaporation flow is then,

$$\dot{M} = 4\pi R^2 n m_O v \simeq 3 \times 10^{-5} \quad M_{\odot}/\text{yr}, \quad (1)$$

where R is the radius of the emitting region (2×10^{17}

cm), n the density (500 cm^{-3}) and m_O the oxygen mass. The lifetime of the clumps is

$$\tau_c = \frac{4\pi R^2 N m_O}{4\pi R^2 n m_O v} = \frac{N_{\text{CO}}}{X_{\text{CO}} n v} = 300 X_{\text{CO}}^{-1} \text{ yr}, \quad (2)$$

with N the column density of the clump. This column density is at least equal to the postshock column density which is equal to $N_{\text{CO}}/X_{\text{CO}}$ with N and X the CO column density and abundance. Observationally, CO is more abundant than O in the postshock gas and this would imply a lifetime of the clumps at least comparable to the lifetime of the remnant. For calculated CO abundances of 10^{-2} (Biscaro & Cherchneff 2014), the expected lifetime is some $3 \times 10^4\text{ yr}$ and the knots may well survive the SNR phase. Finally, we note that the optical knots show variations on a timescale of tens of years (Fesen et al. 2011) and we attribute this to variable geometric structure associated with the heavily corrugated surface of the clumps, reflecting the effects of the Rayleigh Taylor instabilities.

Figure 4 illustrates the structure of the region in a cartoon, identifying the different zones present in this region. The knots are oxygen-rich gas traversed by a $\sim 200\text{ km s}^{-1}$ (reverse) shock. The hot ($\sim 10^6\text{ K}$) gas layer immediately behind the shock is very thin. The optical bright [O III] gas represents the cooling and recombining postshock gas, once the gas has cooled down and recombined, CO is formed and it as well as [O I] are the dominant coolant of this gas. The evaporating surface layers are bright in the IR [O III] lines but not the optical lines. Eventually, this evaporating gas will mix into the dominant X-ray emitting gas that fills the interior of the remnant (Fesen et al. 2011; Patnaude & Fesen 2014). This flux of evaporating gas is driven by heat conduction due to the fast electrons in the X-ray plasma.

The CO/[O I] emitting layers are postshock gas (e.g., material processed by a $\sim 200\text{ km s}^{-1}$ shock) and now cooled down. For the CO/[O I] emitting layers that have a density of 10^{5-6} cm^{-3} , the velocity in the knot (V_k) ranges $6 - 20\text{ km s}^{-1}$ where C-shock is dominated. Grain sputtering requires a velocity greater than 50 km s^{-1} (Draine 1995; Tielens et al. 1994). IR-[O III] emitting regions have a temperature of $\sim 6000\text{ K}$ where no thermal sputtering occurs ($< 10^5\text{ K}$, Biscaro & Cherchneff 2016) and have a counterpart of cold dust when we examined *Herschel* 70 and $160\mu\text{m}$ maps, indicating that dust destruction is not significant. Recent estimates by Nath et al. (2008) and Micelotta et al. (2016) show only 1-20% of grains are sputtered in SN ejecta and the cooling in SN ejecta is rapid due to metal enriched ejecta. This long sputtering timescale as well as the constant reloading of the hot gas with dust from evaporating FMKs may be the reasons that we still observe a significant amount of dust in the hot gas processed by the reverse shock in Cas A. In the end, only those clumps that “survive” the whole SNR expansion phase or that travel beyond the strong shock plowing into the ISM will contribute to seeding the ISM with supernova dust.

In conclusion, SOFIA FIFI-LS observations reveal the morphology of the [O I] and [O III] line emission in the SNR Cas A. The [O I] traces cooled, dense shocked gas and is related to CO emission and dense ejecta. The 52 and $88\mu\text{m}$ [O III] emission reveals a component bright in

the optical [O III] lines with a density of 10^4 cm^{-3} and temperature of 6000 K. This emission is coincident with the dense knots and we associate this with the cooling and recombining postshock gas layer before the gas has cooled down to 500 K and CO has formed. The IR [O III] maps reveal the region with $n \sim 500 \text{ cm}^{-3}$ and $T \sim 6000 \text{ K}$. This gas envelopes the dense knots and we attribute this emission to gas evaporating from the dense knots due to the heat conduction by fast electrons.

We are grateful to Rob Fesen for providing *HST* im-

ages, and Kazik Borkowski for providing helpful comments on the earlier draft. Results in this paper are based on observations made with the NASA/DLR Stratospheric Observatory for Infrared Astronomy (SOFIA). SOFIA is jointly operated by the Universities Space Research Association, Inc. (USRA), under NASA contract NAS2-97001, and the Deutsches SOFIA Institut (DSI) under DLR contract 50-OK-0901 to the University of Stuttgart. Financial support for this work in part was provided by NASA through award SOF-03-0051, issued by USRA.

REFERENCES

- Barlow, M. J., Krause, O., Swinyard, B. M., et al. 2010, *A&A*, 518, L138
- Biscaro, C., & Cherchneff, I. 2014, *A&A*, 564, A25
— 2016, *A&A*, 589, A132
- Borkowski, K. J., & Shull, J. M. 1990, *ApJ*, 348, 169
- Cherchneff, I., & Dwek, E. 2010, *ApJ*, 713, 1
- Colditz, S., Beckmann, S., Bryant, A., et al. 2018, *Journal of Astronomical Instrumentation*, 7, 1840004
- De Looze, I., Barlow, M. J., Swinyard, B. M., et al. 2017, *MNRAS*, 465, 3309
- Docenko, D., & Sunyaev, R. A. 2008, *A&A*, 484, 755
— 2010, *A&A*, 509, A59 (DS10)
- Draine, B. T. 1995, *Ap&SS*, 233, 111
- Ennis, J. A., Rudnick, L., Reach, W. T., et al. 2006, *ApJ*, 652, 376
- Fadda, D., & Chambers, E. T. 2018, in *BAAS*, Vol. 231, , 150.11
- Fesen, R. A. 2001, *ApJS*, 133, 161
- Fesen, R. A., Zastrow, J. A., Hammell, M. C., Shull, J. M., & Silvia, D. W. 2011, *ApJ*, 736, 109
- Fesen, R. A., Hammell, M. C., Morse, J., et al. 2006, *ApJ*, 645, 283
- Hammer, N. J., Janka, H.-T., & Müller, E. 2010, *ApJ*, 714, 1371
- Hurford, A. P., & Fesen, R. A. 1996, *ApJ*, 469, 246
- Itoh, H. 1981, *PASJ*, 33, 521
- Krause, O., Birkmann, S. M., Usuda, T., et al. 2008, *Science*, 320, 1195
- Laporte, N., Ellis, R. S., Boone, F., et al. 2017, *ApJ*, 837, L21
- Matsuura, M., Dwek, E., Meixner, M., et al. 2011, *Science*, 333, 1258
- Micelotta, E. R., Dwek, E., & Slavin, J. D. 2016, *A&A*, 590, A65
- Morse, J. A., Fesen, R. A., Chevalier, R. A., et al. 2004, *ApJ*, 614, 727
- Nath, B. B., Laskar, T., & Shull, J. M. 2008, *ApJ*, 682, 1055
- Nozawa, T., Kozasa, T., Habe, A., et al. 2007, *ApJ*, 666, 955
- Osterbrock, D. E. 1988, *PASP*, 100, 412
- Pagel, B. E. J. 1997, *Nucleosynthesis and Chemical Evolution of Galaxies*, 392
- Patnaude, D. J., & Fesen, R. A. 2014, *ApJ*, 789, 138
- Pei, Y. C., Fall, S. M., & Bechtold, J. 1991, *ApJ*, 378, 6
- Reach, W. T., & Rho, J. 2000, *ApJ*, 544, 843
- Rho, J., Onaka, T., Cami, J., & Reach, W. T. 2012, *ApJ*, 747, L6
- Rho, J., Reach, W. T., Tappe, A., et al. 2009, *ApJ*, 700, 579
- Rho, J., Kozasa, T., Reach, W. T., et al. 2008, *ApJ*, 673, 271
- Rho, J., Gomez, H. L., Boogert, A., et al. 2018, *MNRAS*, 479, 5101
- Sarangi, A., & Cherchneff, I. 2015, *A&A*, 575, A95
- Silvia, D. W., Smith, B. D., & Shull, J. M. 2012, *ApJ*, 748, 12
- Sluder, A., Milosavljević, M., & Montgomery, M. H. 2018, *MNRAS*, 480, 5580
- Spilker, J. S., Aravena, M., Béthermin, M., et al. 2018, *Science*, 361, 1016
- Sutherland, R. S., & Dopita, M. A. 1995, *ApJ*, 439, 381
- Tem, P., Hoffman, D., Ennico, K., & Le, J. 2018, *Journal of Astronomical Instrumentation*, 7, 1840011
- Tielens, A. G. G. M. 2005, *The Physics and Chemistry of the Interstellar Medium*
- Tielens, A. G. G. M., McKee, C. F., Seab, C. G., & Hollenbach, D. J. 1994, *ApJ*, 431, 321
- Wallström, S. H. J., Biscaro, C., Salgado, F., et al. 2013, *A&A*, 558, L2 (W13)